Article

Tunable energy transfer process in heterometallic MOFs materials based on 2,6-naphtalenedicarboxylate: solid-state lighting and near-infrared luminescence thermometry

Germán E. Gomez, Riccardo Marin, Albano N. Carneiro Neto, Alexandre M. P. Botas, Jeffrey Ovens, Alexandros A. Kitos, Maria C. Bernini, Luís D. Carlos, Galo J. A. A. Soler-Illia, and Muralee Murugesu

Chem. Mater., **Just Accepted Manuscript** • DOI: 10.1021/acs.chemmater.0c02480 • Publication Date (Web): 12 Aug 2020

Tunable energy transfer process in heterometallic MOFs materials based on 2,6-naphtalenedicarboxylate: solid-state lighting and near-infrared luminescence thermometry

Germán E. Gomez,[a‡]* Riccardo Marin,[‡b] Albano N. Carneiro Neto,[c] Alexandre M. P. Botas,[c] Jeffrey Ovens,[b] Alexandros A. Kitos,[b] María C. Bernini,[a] Luís D. Carlos,[c] Galo J. A. A. Soler-Illia,[d]* and Muralee Murugesu[b]*

[a] Instituto de Investigaciones en Tecnología Química, Facultad de Química, Bioquímica y Farmacia, Universidad Nacional de San Luis, 5700 San Luis, Área de Química General e Inorgánica, Chacabuco y Pedernera, C.P. 5700 San Luis, Argentina.
[b] Department of Chemistry and Biomolecular Sciences, University of Ottawa, Ottawa, Ontario K1N 6N5, Canada.
[c] Phantom-g, CICECO – Aveiro Institute of Materials, Department of Physics, University of Aveiro, Aveiro Portugal.
[d] Instituto de Nanosistemas. Universidad Nacional de San Martín. Av. 25 de Mayo 1021, San Martín, Buenos Aires, Argentina.

‡ These authors contributed equally to this work

ABSTRACT: Trivalent lanthanide ions (Ln^{3+}) are used to prepare a plethora of coordination compounds; metal-organic frameworks (MOFs) being amongst the most sought-after in recent years. The porosity of Ln-MOFs is often complemented by the luminescence imparted by the metal centers, making them attractive multifunctional materials. Here, we report a class of 3D MOFs obtained from solvothermal reaction between 2,6-naphtalenedicarboxylic acid (H_2NDC) and lanthanide chlorides yielding three types of compounds depending on the chosen lanthanide: [LnCl(NDC)(DMF)] for Ln^{3+} = La^{3+}, Ce^{3+}, Pr^{3+}, Nd^{3+}, Sm^{3+} (type 1), $[Eu(NDC)_{1.5}(DMF)]\cdot 0.5DMF$ (type 2), and $[Ln_2(NDC)_3(DMF)_2]$ (type 3) for Ln^{3+} = Tb^{3+}, Dy^{3+}, Y^{3+}, Er^{3+}, Yb^{3+}. Photoluminescent properties of selected phases were explored at room temperature. The luminescence thermometry capability of Yb^{3+}-doped Nd-MOF was fully investigated in the 15-300 K temperature range under 365 and 808 nm excitation. To describe the optical behavior of the isolated MOFs, we introduce the *total energy transfer balance* model. Therein, the sum of energy transfer rates is considered along with its dependence upon the temperature: sign, magnitude, and variation of this parameter, permitting to afford a thorough interpretation of the observed behavior of the luminescent species of all materials presented here. The combination of novel theoretical and experimental studies presented herein to describe energy transfer processes in luminescent materials can pave the way towards the design of MOF-based chemical and physical sensors working in an optical range of interest for biomedical applications.

Introduction

Metal-Organic Frameworks (MOFs) are composed of metal ions connected by organic ligands, yielding a plethora of open structures with unique crystalline architectures.[1,2] The combination of MOF open porosity with the specific electronic or optical properties leads to multifunctional materials that have attracted the attention for applications in fields such as gas storage,[3] photoluminescence,[4] heterogeneous catalysis,[5,6] ion-exchange,[7] and drug delivery.[8]

Seeking photoluminescence (PL) properties, trivalent lanthanide ions (Ln^{3+}) are optimal species for the preparation of MOFs, since they can impart tailored emission properties spanning a broad wavelength range: from ultraviolet to visible and near-infrared (NIR). Importantly, variations of the PL spectral profile induced by environmental changes can be harnessed for sensing purposes or sensitizing. Indeed, the intrinsic porosity accompanied by the large surface area of MOFs offer great opportunities for exploiting the intermolecular interaction between the framework and guest molecules, which can dramatically vary the coordination environment and harnessing energy transfer processes, thus modulating the luminescent properties of MOFs.[9] Besides, the structure of MOFs can be further modified post-synthesis, thus enabling fine-tuning of a specific luminescence response.[10] In comparison to traditional luminescent organic molecules and coordination compounds, MOFs also have the advantage to feature a periodic disposition of the luminescent centers; this enables long-range interactions, thus favoring the development of new functionalities, such as waveguide effects.[11,12,13]

Therefore, the design of optically active MOFs is pivotal for sensor development.[14,15,16,17] Indeed, there are plenty of examples of structures suitable for the selective detection of toxic species in aqueous environments,[18] explosives,[19] metallic ions[20] and many more molecules.[21]

In this vein, the possibility to accurately measure temperature through optical signals is crucial for understanding biological, chemical, and physical processes. Optical temperature measurement is a valid alternative to traditional contact thermometry methods such as those employing bimetallic thermometers, liquid-filled glass thermometers, thermistors and thermocouples.[22] Optical thermometers offer the possibility of non-contact measurement, and measurement at the submicron scale, an

exciting opportunity for intracellular applications. Conveniently, luminescent thermometers offer the possibility to work in a non-invasive and accurate way.[23]

Pioneering work by Qian[24] and some of us[25,26] have promoted intense research around mixed-lanthanide MOFs capable of acting as luminescent thermometers over different temperature ranges.[27,28,29,30,31,32,33] Those mixed Eu^{3+}/Tb^{3+} MOF thermometers are limited by their luminescence in the visible region,[34,35] but NIR luminescent MOFs can be also designed for temperature sensing. Such NIR luminescent MOFs are useful for biological applications, due to the existence of so-called "optical transparency windows" – NIR wavelength ranges where tissue-induced light extinction is minimized.[36] Surprisingly, there are fewer studies focusing on MOF-thermometers with NIR operation capabilities and extended temperature working range.[37,38,39] There is an enormous potential for NIR-luminescence thermometry in early detection of diverse diseases, such as stroke, inflammation processes or even cancer, one of whose incipient symptoms is the appearance of temperature singularities localized in the affected tissues.[40] In all those instances, NIR-operating MOFs with temperature-sensitive emission could be foreseeably employed to garner indirect information about the health of biological systems.

Clearly, more investigations around NIR-luminescent MOFs operating in that spectral range are needed, in order to lay the foundations for the development multifunctional materials. In the biomedical context, for instance, those systems could simultaneously afford optical imaging and report on the thermal state of the site of interest, as well as deliver drugs loaded in their pores. This powerful combination makes NIR-luminescent MOFs credible candidates for theranostic applications[41,42,43,44,45,46] (i.e., combining therapy and diagnosis).

From the design point of view, 2,6-naphtalenedicarboxylate (H_2NDC) has been employed as suitable ligand for preparing MOFs based on lanthanides[47,48,49,50,51,52] or d-block elements.[53]

In this work, we showcase a new set of 3D-frameworks based on H_2NDC and Ln^{3+} ions–from La^{3+} to Yb^{3+} (save Pm^{3+}, Gd^{3+}, Ho^{3+} and Tm^{3+}) yielding three sets of structures. These were classified in type 1 [Ln(NDC)Cl(DMF)] (Ln^{3+} = La^{3+}, Ce^{3+}, Pr^{3+}, Nd^{3+}, Sm^{3+}), type 2 $[Eu(NDC)_{1.5}(DMF)]\cdot 0.5DMF$, and type 3 $[Ln_2(NDC)_3(DMF)_2]$ (Ln^{3+} = Tb^{3+}, Dy^{3+}, Y^{3+}, Er^{3+}, Yb^{3+}) phases. An in-depth photophysical characterization highlighted the aptness of NDC^{2-} to act as antenna, *i.e.*, to absorb and funnel the excitation energy to the emitting levels of Ln^{3+} ion such as Eu^{3+}, Sm^{3+} and Nd^{3+}. Mixed Nd-Yb MOFs were synthesized and their behavior as ratiometric NIR-emitting luminescent thermometers was ascertained. Upon choosing the convenient integration intervals, the results indicated an extended temperature working range (15-300 K) under both UV and NIR excitation. This versatility suggests the possibility of performing temperature sensing using the presented system depending on the boundaries given by temperature of interest and most convenient excitation source. To model the optical behavior of the synthesized MOFs, the concept of total energy transfer balance $W^*(T)$ was introduced. These results drive the perspectives to develop temperature sensors for biological media, which in turn has great impact as the last generation of diagnostics and therapeutic strategies.

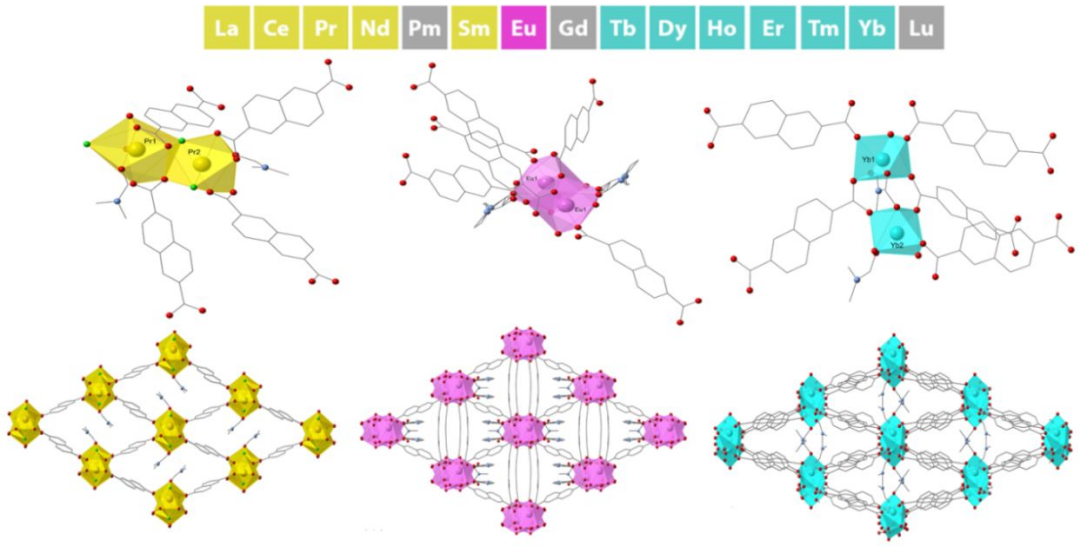

Figure 1. "Ball and stick" representation of the asymmetric unit of the three type of compounds and the corresponding projections of each structure along the *b* axis.

Results and discussion

Three types of Ln-MOF were synthesized and isolated upon solvothermal synthesis (Figure 1). A description of the structural features is presented as follows.

Type 1 compounds. Type 1 (**La** – **Sm**) compounds present the general formula [Ln(NDC)Cl(DMF)]. The structural description will be made based on compound Pr-MOF (**Pr**) meanwhile specific information about **Ce** will be given when necessary. The compounds crystallize in the monoclinic $P2_1/c$ space group; the cell parameters for both compounds are shown in Table S1. In the asymmetric unit there are two crystallographically non-equivalent Ln^{3+} ions, both nona-coordinated, and one independent NDC^{2-} anion (see Figure 2, S1, S3). Pr1 and Pr2 are surrounded by six oxygen atoms coming from carboxylate groups, one oxygen atom from a DMF molecule and two chloride atoms. The coordination geometry of both metal centers is consistent with a

monocapped square antiprism. The Pr1-O bond lengths fall in the range 2.438(3) - 2.689(2) Å whereas the Pr2-O ones are in the range 2.426(3) - 2.645(2) Å. Meanwhile Pr-Cl distances fall into the range 2.870(1) - 2.894(1) Å. In the case of **Ce**, the corresponding distances are between 2.455(3) - 2.703(3) Å for [Ce1-O] polyhedron and between 2.442(3) - 2.663(3) Å for the [Ce2-O] one. Both set of distances are in agreement with Ln-O distances in MOFs based on "early" lanthanide ions (Pr, Sm).[54]

The ligand links two metal ions by each carboxylate group in a chelate-bridge fashion (Figure S3). Besides, the Secondary Building Unit (SBU) runs along the *b* direction and consists of chains of [PrO_7Cl] edge-sharing coordination polyhedra (Figure 1). The chains are connected along the *c* direction by one NDC^{2-} ligand (Figure S4).

Type 2 compound. Under same synthetic conditions but employing Eu metal source, a mixture of unknown phases is obtained (see Experimental Section) By a slight increment of the ligand concentration with respect to the synthesis of type 1 series, single crystals of [$Eu(NDC)_{1.5}(DMF)$]·0.5DMF were obtained (**Eu**). The compound is structurally similar to the previously obtained Ce-phase,[47] [$Ce(NDC)_{1.5}(DMF)(H_2O)_{0.5}$]·0.5DMF (Ce-FJU6). The asymmetric unit is composed by one crystallographic independent europium center surrounded by seven oxygen atoms from NDC ligands and one from the DMF (Figure 1 and S5). The Eu-O bond distances in each [EuO_8] polyhedra central fall in the 2.261(2)-2.498(7) Å, regularly seen in Eu-based carboxylates.[8] The SBU is consisting on chains of dimmers of [EuO_8] polyhedral running along *c* direction, which are connected by NDC^{2-} ligands in two directions (Figure S6). Moreover, there are two ligand types that coordinate four metal ions. One of them coordinates two europium ions by each carboxylate group in a chelate-bridge fashion; meanwhile the other linker exhibits a bidentate-bridge coordination by its two carboxylates extremes (Figure S3). Besides, it is remarkable that another difference between **Eu** and the previously reported Ce-FJU6, is the way in which the dimmers are connected being only carboxylates bridges. For the case of the later phase, the dimmers are connected between them by carboxylates and water molecules (Figure S7). The fact of having water-bridges reinforcing the chains dimmers is due to the lower temperature synthesis (95 ºC) and the use of water in the corresponding synthesis,[47] respect to that of **Eu**.

Type 3 compounds. Type 3 (**Tb** – **Yb**) compounds are described as follows. In this case, [$Yb_2(NDC)_3(DMF)_2$] (**Yb**) is used for structural description as representative of this sets of MOFs. It crystallizes in the monoclinic $P2_1/c$ space group; the asymmetric unit contains two non-equivalent Yb^{3+} ions, and also three NDC ligands exhibiting a bridge-bidentate fashion (Figure 1 and S8). The coordination environment around Yb1 and Yb2 ions involves six oxygen atoms coming from carboxylate groups and one oxygen from the carbonyl group of one DMF molecule. The isolated polyhedra are linked together by carboxylate groups, forming 1D chains along *c* direction (SBU), and are further connected through the organic linkers giving rise to 3D structure (see Figure S9). The Yb1-O bond lengths fall into the 2.221(7)-2.301(6) Å meanwhile Yb2-O ones are in the 2.195(5)-2.358(7) Å, which are consistent with that of previously reported succinate-containing ytterbium MOF.[55] Basing on the organic-inorganic connectivities in type 1 and type 2 compounds can be classified as I^1O^2, where I^1 means that the inorganic connectivity is 1D and O^2 implies that the organic one is 2D, which involves organic linkers connecting the SBUs in two crystallographic directions; the sum of the exponents gives the overall dimensionality of the structure. Meanwhile, type 3 compounds exhibit I^0O^3 connectivity, since the inorganic connectivity is 0D due the presence of isolated polyhedral, which are connected in all the space by organic linkers.

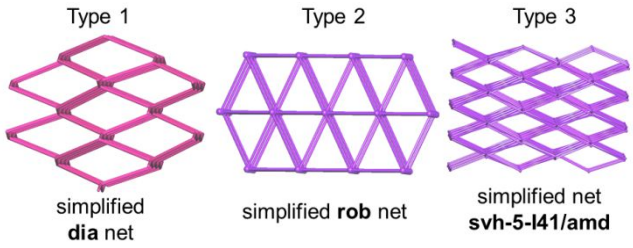

Figure 2. Projection of the simplified nets in the three type of MOFs.

The porosity of two representative compounds, **Nd** and **Yb**, were further investigated. Using a probe radius of 1.2 Å in Mercury, solvent accessible voids were calculated to be 970.03 and 789.29 $Å^3$, accounting for 30.2 and 20.6% of the crystal volume, for **Nd**- and **Yb**-MOFs, respectively.[56] Gas adsorption measurements were also performed (details in ESI). Upon activation at 360 ºC, **Nd** changed color (Figure S10) and displayed low N_2 uptake (3.347 cm^3/g - type-II profile with type H3 hysteresis loops associated with multilayer systems) and small BET surface area 1.992 m^2/g (Figure S11). Given the thermal stability of **Nd** at that temperature (Figure S14) we ascribe this behavior to a phase transition. Activated **Yb**-MOF exhibited instead an N_2 uptake of 70.268 cm^3/g (Figure S11), with BET and Langmuir surface areas of 201.95 and 292.659 m^2/g, respectively. The N_2 adsorption isotherm showed a type-I(b) profile indicative of the microporous nature of the framework.[57] Indeed, **Yb**-MOF featured an average pore size of 3.87 Å (Figure S12 - calculated using the Horvath-Kawazoe method), in agreement the value of 3.93 Å calculated using the Non-Local Density Functional Theory (NL-DFT) method.

Topological analysis

The compounds here reported, belonging to three different structural types, have been analyzed from a topological viewpoint by using the TOPOSPRO program.[58] As we described recently,[59] this code allows for obtaining the underlying net of a metal-organic framework structure or organic molecular crystals with hydrogen-bonded networks by carrying out two types of structural simplifications, i.e., the standard or cluster simplification procedures.

The first one takes into account the connectivity of each ligand and metal center and is more suitable to be applied when the inorganic SBU is composed of isolated polyhedra. The second one considers the SBU as a node and the structure is described in terms of the connectivity among these nodes and the organic linkers.[60,61] Four deconstruction methods to obtain the underlying net were recently described by Bonneau et al.[62] being Method 4 here applied as follows.

Different dimensions of the condensation of polyhedra are identified; i.e., 1D chains in type 1, dimeric units in type 2 and

isolated polyhedra in type 3; however, in all structural types there is a crystallographic direction in which the inorganic polyhedra are closer than in the other two ones forming 1D-tertiary building units (TBUs)[63] or supramolecular building blocks (SBBs)[64]. In type 1 this fact occurs because the polyhedra link together by sharing faces forming 1D chains; in type 2, the binding between polyhedra is achieved by sharing edges and alternatively by COO- groups, forming 1D chains of dimeric units (1D TBU), and in type 3, the inorganic chain is built through COO- groups only forming also a 1D TBU (see Figure S13).

For this reason, all structures were simplified preserving the inorganic SBU or TBU entity, analyzing their packing as construction modules. To this end, occasionally a ghost atom has been introduced into these SBUs, as it is depicted in Figure S13, and simplified uninodal nets were obtained in all cases. By this procedure, type 1 frameworks can be described as a 4-connected uninodal net **dia** type (Point Schläfli symbol for the net 44), type 2 frameworks as 6-connected net of the **rob** type topology (Point Schläfli symbol for the net $4^8.6^6.8$), and type 3 as a 5-connected net **xbj**; **svh-5-I41/amd**, being the Point Schläfli symbol for this net $4^4.5^5.6$.

Optical properties

Single-lanthanide MOFs. The PL emission of selected systems was first probed under UV excitation (Figure 3A). Most of the MOFs present a broad-band feature spanning the 400-600 nm range. This feature stemmed from $\pi^*\rightarrow\pi$ transitions taking place in NDC^{2-}, as confirmed by the comparison with the emission of the pristine ligand under the same excitation. The characteristic visible emission lines of Eu^{3+}, Sm^{3+} and, less intensely, Tb^{3+} were observable. Similarly, **Dy** showed very dim Dy^{3+} emission lines superimposed to broad ligand-centered photoluminescence (Figure S17). **Nd** did not show any Nd^{3+} visible emission, its spectrum resembling that of the MOF based on non-emitting La^{3+} (Figure 3B). Nonetheless, Nd^{3+} NIR emission, originating from $^4F_{3/2}\rightarrow{}^4I_{11/2}$ and $^4F_{3/2}\rightarrow{}^4I_{13/2}$ transitions, was observed (Figure 3C). The sensitization of Eu^{3+} and Sm^{3+} luminescence, along with the inefficient population of Tb^{3+} $^5D_4$ state, suggested that the NDC^{2-} triplet state lied just above the emitting level of this latter Ln^{3+} ion (Figure 3D). This assumption was confirmed by theoretical calculations, which returned a triplet state (T_1) energy of approximately 22500 cm^{-1} (see ESI).

In order to gain full knowledge on the energy transfer (ET) mechanism between the lanthanide ions and the ligand, we developed and herein propose the *total energy transfer balance* (*W**) model. This model is based on the theory given in Refs.[65,66,67,68,69,70,71,72] and it considers the summation over all possible ET rates both in the case of positive and negative energy difference between metal and ligand singlet and triplet states (see details in ESI). Remarkably, this model easily explains why **Tb** MOF presents a sizeable ligand emission (Figure 3E). In particular, this can be ascribed to the fact that pathway 3 in **Tb** MOF has a high backward ET rate to the S_1 ligand state, while in **Eu** and **Sm** systems the ligand-to-metal ETs are dominant (see also Tables S3-S8).

Heterometallic MOFs. Given that Eu^{3+} salts are substantially more expensive (50-100 times) compared to optically inactive La^{3+}, we showed that bright red emission is preserved in mixed La-Eu MOFs (Figure S18). This approach also allowed producing a unique phase structure (type 1), while in **Eu** (type 2) two structures co-existed. The presence of a single-phase makes the system better suited for applications requiring a full understanding and interpretation of the emission spectrum. Following the same rationale, **La** MOFs doped with an increasing amount of Nd^{3+} as the luminescent center was synthesized (Figure 4). Both **La** and **Nd** belong to type 1 compounds, ensuring compositional tuning over the whole 0-100% Nd^{3+} content (Figure S19). This study was conducted in an attempt to maximize the NIR emission intensity under 808 nm excitation.[73,74,75,76,77,78] In general, it is desirable to maximize the Nd^{3+} content, so to improve the light absorption capability of the system–which is not necessary in case of ligand-sensitized PL. However, an excessive concentration of Nd^{3+} ions in close proximity usually results in concentration quenching due to cross relaxation and energy migration phenomena.[79,80]

From the absorption spectra recorded on the series of synthesized samples (Nd^{3+} content = 0, 3, 5, 10, 20, 40, 100%), the enhancement of the absorption properties in the NIR range due to the direct Ln^{3+} light absorption is evident. Surprisingly enough, it was found that Nd^{3+} emission intensity increased linearly with the metal ion content in the MOF, showing no sign of concentration quenching under 808 nm excitation (Figure 4B).

With this knowledge in hand, we selected the pure **Nd** MOF as a basis to prepare mixed MOFs containing both this lanthanide ion and Yb^{3+}. In fact, the energy transfer (ET) among this pair of ions is known to afford luminescence thermometry over different temperature ranges.[81] Attempts to dope Yb^{3+} in the lattice at increasing concentrations showed that 5% was the maximum value achievable (powder X-ray diffraction patterns in Figure S20). This threshold was imposed by the limited solubility of the latter ion in the **Nd** lattice (type 1), since **Yb** crystallized in a different crystal phase (type 3). Therefore, when doping with higher Yb^{3+} content was attempted, mixed-phase samples were obtained (not shown). The three synthesized Yb^{3+}-doped **Nd** MOFs (1, 2.5 and 5%) displayed the characteristic NIR Yb^{3+} and Nd^{3+} emission both under UV (365 nm) and NIR (808 nm) excitation (Figure S21). This two-fold means to foster NIR emission from the two Ln^{3+} ions simultaneously is guaranteed by the energy transfer mechanisms taking place between the two luminescent centers.[82] The use of Nd^{3+} as a NIR energy harvester (sensitizer) is a common approach in the field of lanthanide-based luminescent materials, owing to its large light absorption cross-section. Nd-to-Yb ET takes place also when Nd^{3+} excited states are populated following ligand excitation, rather than through direct Ln^{3+} excitation. The result is the appearance of three emission bands in the NIR originating from Yb^{3+}: $^2F_{5/2}\rightarrow{}^2F_{7/2}$, Nd^{3+}: $^4F_{3/2}\rightarrow{}^4I_{11/2}$, and Nd^{3+}: $^4F_{3/2}\rightarrow{}^4I_{13/2}$ transitions centered respectively at 980, 1050 and 1350 nm (Figure S21).

The emission of the mixed MOFs was investigated in the 15-300 K temperature range both under 365 and 808 nm excitation (Figures 5A, 5C, S22, and S23). A clear difference in the relative emission intensity was observed between Nd^{3+} and Yb^{3+} emission when the MOF was irradiated with the two wavelengths. Under 808-nm excitation, the energy transfer from Nd^{3+} to Yb^{3+} is the only responsible for the population of the emitting state of the latter ion. Instead, under UV excitation, Yb^{3+}: $^2F_{5/2}$ level is fed directly from the ligand (NDC^{2-}) and from the indirectly excited Nd^{3+} ion (Figure 5E).

It is also important to mention that the energy transfer between the Yb^{3+}-Nd^{3+} ion pair entails thermally activated forward (Nd-to-Yb) and back transfer (Yb-to-Nd) processes. They depend on the phonon energy of the system and the temperature range explored.[78] Moreover, intensity changes in the fine structure of individual transitions generally take place due to the electron population re-distribution between Stark sub-levels of the lanthanide emitting state (Figure 5F).[83,84,85]

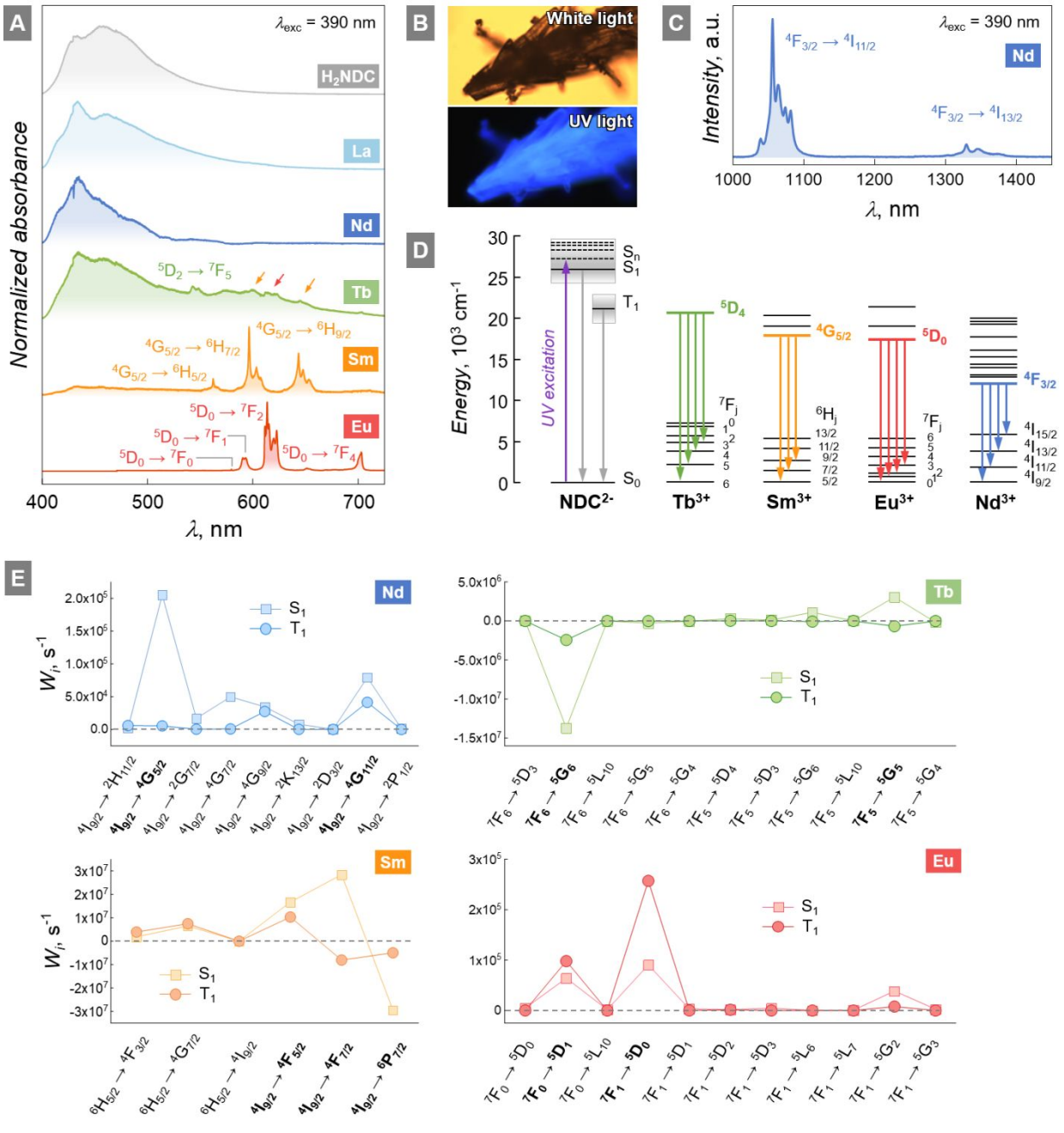

Figure 3. **A**: Visible emission properties under UV excitation (λ_{exc} = 390 nm) of selected MOFs prepared in this study. Orange and red arrows in **Tb** spectrum indicate emission stemming from Sm^{3+} and Eu^{3+} impurities, respectively. **B**: **La** crystals under white and UV illumination as observed under a microscope. **C**: NIR emission of **Nd** under the same UV excitation. **D**: Partial energy level scheme of the ligand and selected lanthanide ions as derived from the comparison of the obtained emission spectra reported in **A**. **E**: Values of ET rates (W_i) for the more relevant pathways in each MOF investigated in this work (Ln = Nd, Tb, Sm and Eu). All the pathways and individual rates can be found in Tables S4-S7. The temperature was considered constant (T = 300 K). Squares and circles represent ET rates involving the S_1 and T_1 states, respectively. Negative values (points below the dashed grey lines) indicate that the ET occurs from the Ln^{3+} ion to the ligand (backward ET). The transitions highlighted in bold are those more decisively contributing to the overall ET rate.

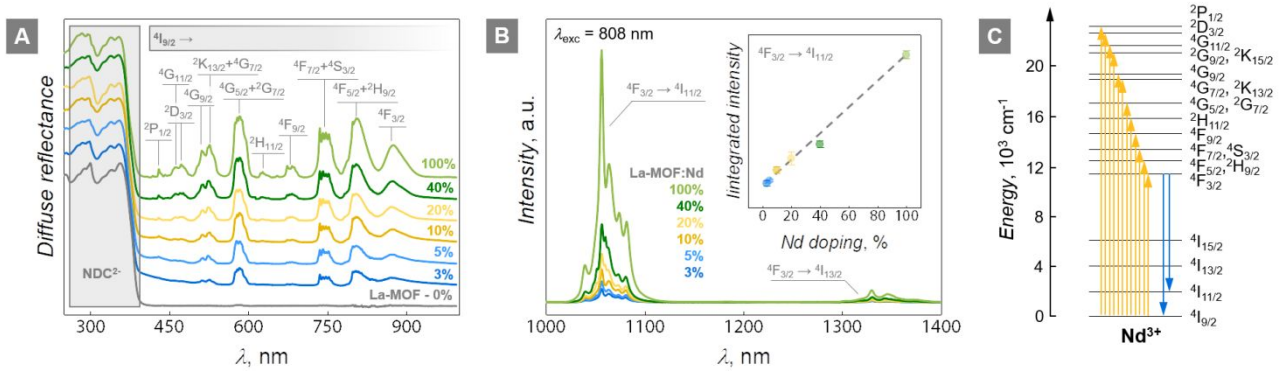

Figure 4. **A**: Absorption spectra of a series of **La** MOFs doped with increasing percentage of Nd^{3+}, up to 100% (i.e., pure **Nd** MOF). **B**: emission spectra of the same series of samples under 808 nm excitation. In the inset the linear trend of the $^4F_{3/2}\rightarrow{}^4I_{11/2}$ band integrated intensity is reported. **C**: partial energy level scheme of Nd^{3+}, where the absorption (yellow) and emission (blue) lines observed in **A** and **B** respectively are indicated.

The total energy transfer balance model affords an accurate explanation of the optical behavior of the system (Figure 5G). The trend of *Yb/Nd* emission intensity ratio is analogous both under 365 and 808 nm excitation (Figures 5H and S24). *Yb/Nd* intensity ratio stays approximately constant below 100 K, to then increase throughout the 100-300 K temperature interval. This trend can be explained considering only ET processes from Nd^{3+}: $^4F_{3/2}$ level. This assumption is supported by the calculated fast multiphonon relaxation rates found from higher energy levels of Nd^{3+} to lower lying ones, which quickly leads to Nd^{3+}: $^4F_{3/2}$ level population. For instance, the relaxation rate from $^4F_{5/2}$ to $^4F_{3/2}$ (approx. $3\cdot10^5$ s^{-1}) is 15 times higher than the Nd^{3+}: $^4F_{3/2}\rightarrow Yb^{3+}$: $^2F_{5/2}$ ET rates (the sum of pathways 1 and 16 is approx. $2\cdot10^4$ s^{-1}, Figure 5G and Table S8). Moreover, the lack in the recorded spectra of Nd^{3+}: $^4F_{5/2}\rightarrow{}^4I_{11/2}$ emission (normally found around 950 nm)[86] further corroborates the efficient depopulation of higher energy levels. All this considered, as seen in Figure 5H, to model the emission of mixed MOFs it is sufficient to consider transitions $^4F_{3/2}\rightarrow{}^4I_{9/2}$ (pathway 1) and $^4F_{3/2}\rightarrow{}^4I_{11/2}$ (pathway 16) of Nd^{3+} as donors.

Luminescence thermometry. All above considered, in the mixed MOFs under study there are several spectral variations occurring simultaneously due to temperature changes. These variations can be harnessed to obtain information about the thermal state of the system (luminescence thermometry). One of the most reliable ways to achieve luminescence thermometry is to consider as the thermometric parameter the luminescence intensity ratio (*LIR*) between signals integrated over conveniently chosen wavelength ranges. This approach allows to overcome the shortcomings related to non-ratiometric methods (*e.g.*, fluctuations in intensity, concentration, and power fluctuations of the excitation source). We report here the case of the 5% Yb^{3+}-doped **Nd** MOF. Some other selected examples of thermometry with MOFs doped at 1 and 2.5% are reported in the Supporting Information (Figure S22 and S23). The stronger luminescence under 365 nm excitation allowed the use of measurements conditions that made it possible to clearly resolve Stark components within the Nd^{3+}: $^4F_{3/2}\rightarrow{}^4I_{11/2}$ manifold (Figure 5A). Hence, *LIR* (I_2/I_1) was obtained as the ratio between the integrated intensity of the two components centered at 1082 (I_2) and 1066 nm (I_1). When 808 nm excitation was employed, different integration ranges were selected, with Yb^{3+} emission also being considered (Figure 5C). Both *LIR* datasets were fit linearly and the slope of the line (*i.e.*, its first derivative) was used to retrieve the relative thermal sensitivity according to the following equation: [87]

$$S_r = \frac{1}{LIR}\frac{\partial LIR}{\partial T} \qquad (1)$$

The resulting sensitivities (Figure 5B and 5D) varied between approximately 0.1 and 0.2 % K^{-1}, being highest approaching room temperature. These values are close to those reported for systems based on mixed Nd^{3+}-Yb^{3+} systems[79,80] and other singly doped with or Nd^{3+}.[73-77] Importantly, the associated temperature uncertainty (see Eq. 1) remained below 0.2 and 1 K when using 365 or 808 nm excitation routes, respectively. Similar performance was displayed by the **Nd** MOFs doped with lower amounts of Yb^{3+} (Figure S22 and S23), the highest relative sensitivity being showcased by the 1% Yb^{3+} doped MOF under 808 nm excitation (approx. 0.25 % K^{-1} at 300 K).

The possibility to probe the temperature utilizing two different thermometric parameters that can be summoned via orthogonal excitation (either UV or NIR), is a remarkable advantage since it allows using one approach to cross check the accuracy of the temperature measured with the other, and vice versa.

Conclusions

Three types Metal-Organic Frameworks (MOFs) based on lanthanides and 2,6-naphtalenedicarboxylic acid (H_2NDC) were obtained *via* a solvothermal method. Depending on the lanthanide ion, the compounds have the following chemical formulae: [LnCl(NDC)(DMF)] (Ln^{3+} =La^{3+}, Ce^{3+}, Pr^{3+}, Nd^{3+}, Sm^{3+}) (type 1), [Eu(NDC)$_{1.5}$(DMF)]•0.5DMF (type 2), and [Ln_2(NDC)$_3$(DMF)$_2$] (type 3) (Ln^{3+} = Tb^{3+}, Dy^{3+}, Y^{3+}, Er^{3+} and Yb^{3+}). The crystal structure was solved for Pr, Ce, Eu and Yb MOFs by means of single-crystal X-ray diffraction: it was found that the compounds crystallize in the monoclinic space group $P2_1/c$ (type 1 and 3) or $C2/c$ (type 2). Type 1, 2 and 3 compounds are 3D frameworks consisting of chains of [LnO_7Cl] (type 1), [LnO_7]/[LnO_8] (type 2) or [LnO_7] (type 3) polyhedra, respectively, linked by dicarboxylate anions. From the topological point of view, the 3D frameworks were

simplified as **dia**, **rob** and **svh-5-I41/amd**, where 4-, 6- and 5-connected nets were found for type 1, 2 and 3.

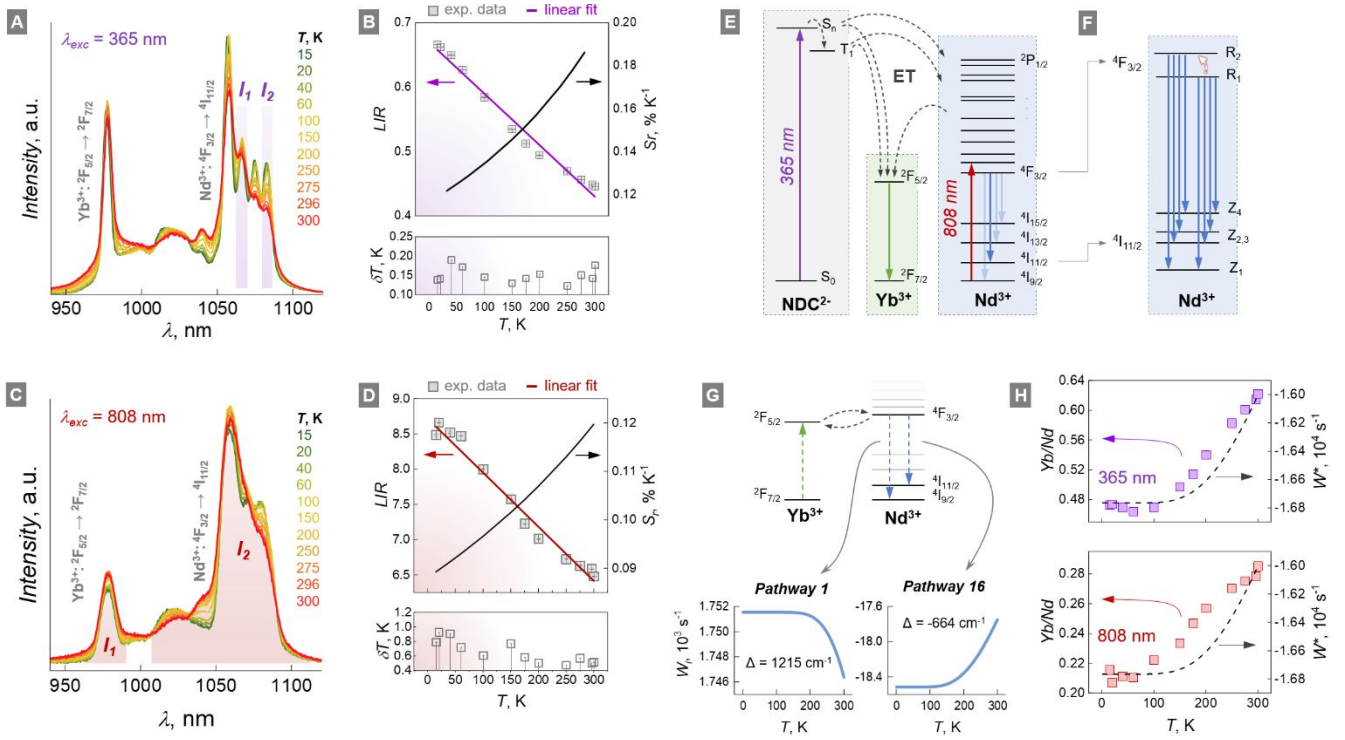

Figure 5. The temperature-dependent emission spectra of the mixed MOF (5% Yb^{3+}-doped **Nd** MOF) in the 940-1120 nm range under 365 and 808 nm excitation are reported in **A** and **C**, respectively. There, the integration ranges utilized to then obtain the two *LIRs* (I_2/I_1) are highlighted. In **B** and **D**, the dependence of *LIR* on the temperature (experimental points – grey squares), the corresponding linear fit (colored straight lines – r^2=0.978 and 0.973, respectively) and the relative thermal sensitivities are reported along with the temperature uncertainties. **E**: Partial energy level scheme of the Yb-doped Nd-MOF. The two excitation routes (UV – 365 nm; NIR – 808 nm) are indicated, along with the energy transfer processes responsible for the population of the emitting states of Yb^{3+} and Nd^{3+}. In **F**, a zoom/in of the transitions between Stark sublevels of Nd^{3+}: $^4F_{3/2}$ and $^4I_{11/2}$ states are presented. The red glowing arrow indicates the thermally activated electron population redistribution within Stark sublevels. **G**: behavior of the energy transfer rate W_i as a function of the temperature for $^4F_{3/2} \rightarrow {}^4I_{9/2}$ (pathway 1) and $^4F_{3/2} \rightarrow {}^4I_{11/2}$ (pathway 16) of Nd^{3+} as donors (see also Table S8). **H**: comparison between W^* as a function of temperature (Eq. 4) for the Nd^{3+}-Yb^{3+} energy transfer considering the sum of the abovementioned pathways (dashed lines) and the intensity ratio between Yb^{3+} $^2F_{5/2} \rightarrow {}^2F_{7/2}$ and Nd^{3+} $^4F_{3/2} \rightarrow {}^4I_{11/2}$ emissions under 365 nm (purple squares) and 808 nm excitation (red squares). The model well predicts the behavior of the system, with an increase of the relative Yb^{3+} emission compared to Nd^{3+} taking place above 100 K.

The photoluminescence properties from MOFs based on La^{3+}, Nd^{3+}, Sm^{3+}, Tb^{3+} and Eu^{3+} were investigated in detail, observing different efficiency in the lanthanide emission through ligand sensitization. We further prepared near-infrared (NIR)-emitting Nd-MOFs doped with different amounts of Yb^{3+} and studied their temperature-dependent NIR emission. The energy transfer between the ligands and the two metal centers, along with electron population redistribution withing Stark sublevels, afforded thermal readouts in the 15-300 K range both under UV and NIR excitation. The best thermal sensitivity under 365 and 808 nm excitation wavelengths were 0.19 and 0.25 % K^{-1}, respectively.

The behaviors of both single lanthanide and heterometallic Ln-MOFs were modeled introducing the concept of *total energy transfer balance, W**. Using this model, the luminescence of the Ln-based systems can be understood and foreseen considering the sum of the energy transfer rates over all the energy transfer pathways between energy donors and acceptors species.

The introduction of a new and applicable theoretical model to describe energy transfer processes in this type of system opens a new possibility in the landscape of optically active lanthanide materials, in which optical properties can be designed in terms of the Ln composition. These results are promising for the design of NIR-operating MOFs with thermal sensing capabilities – especially interesting for biological applications.

Methodology

Chemicals

All chemicals were purchased from Alfa Aesar, STREM Chemicals, Ark Pharm, and Sigma Aldrich and were used as received without further purification.

General procedures for the synthesis of Ln-MOFs

All the compounds were prepared under almost identical solvothermal synthesis conditions, by dissolving 2,6-naphtalendicarboxylic acid (0.4 mmol) and the lanthanide chlorides (0.4 mmol) in 5 mL of N,N'-dimethylformamide (DMF). After stirring for 30 minutes, the resultant mixtures were heated at 150 °C in a 23 mL Teflon-lined Parr bomb during 48 hours; then, the reactors were immediately cooled to room temperature and the crystalline powders were washed with 10 mL of DMF, filtered and dried at room temperature.

Crystals suitable for single-crystal X-ray diffraction analysis could be carefully isolated for Ce, Pr, Eu and Yb. Detailed procedure can be found in Supp. Inf.

Purity of the samples was confirmed by comparison of the experimental and simulated powder XRD patterns (see Figures S30-33).

Following the reaction shown in Scheme 1, crystalline samples were obtained as prismatic bulk crystals. This morphology, observed by SEM is shown in Figure S34.

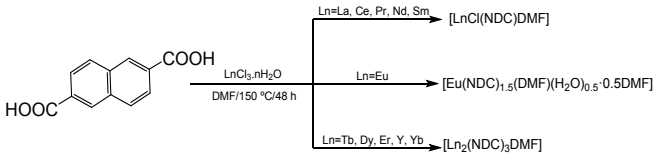

Scheme 1: Synthesis of the Ln-MOFs reported herein.

Characterization methods

Single-crystal X-ray diffraction analysis, the crystals were mounted on thin glass fiber, affixed using paraffin oil, and cooled to 200.15 K. Subsequently, data were collected on a Bruker AXS SMART or KAPPA single-crystal diffractometer equipped with a sealed Mo tube source (λ = 0.71073 Å) and APEX II CCD detector. The data reduction included multi-scan absorption correction (SADABS). Raw data collection and processing were performed with APEX II software package from BRUKER AXS. The crystal structures were solved and refined using the SHELXTL program suite (v. 2012, A. S. S.; Bruker AXS: Madison, W., 2005). Direct methods were used yielding all non-hydrogen atoms, which were refined with anisotropic thermal parameters. All hydrogen atom positions were calculated based on the geometry of their respective atoms. Data collection results represent the best data sets obtained in several trials for each structure. A summary of conditions for data collection and structure refinement is given in Table S1.

Powder XRD patterns of all compounds were recorded using a Rigaku Ultima IV Diffractometer with Cu-Kα radiation (λ_1= 1.54056 Å, λ_2= 1.54439 Å) operating at 40 kV and 40 mA. MERCURY 2.0[56] and CrystalMaker[88] programs were used for molecular graphics for publication.

Thermogravimetric analysis (TGA), differential thermal analysis (DTA), were performed with Shimadzu TGA-51, and DTA-50 apparatus under flowing air at 50 mL min^{-1} and a heating rate of 10 °C min^{-1}. TGA/DTA data is depicted in Figures S13-15 and Table S2.

The adsorption isotherms for N_2 (Ultrahigh purity) were conducted using an Accelerated Surface Area & Porosimetry System (ASAP) 2020 supplied by Micromeritics Instruments Inc. A liquid N_2 bath was used for adsorption isotherms at 77 K.

Visible emission spectra were obtained at room temperature with a custom-built hyperspectral microscope (IMA UpconversionTM by PhotonEtc) equipped with an inverted optical microscope (Nikon Eclipse Ti-U), a Nikon Halogen Lamp (IntensiLight 100 W) with a single band DAPI filter cube for 390 nm UV excitation, a broadband camera for color imaging, a set of galvanometer mirrors, a Princeton Instruments SP-2360 monochromator/spectrograph, and a Princeton Instruments ProEM EMCCD camera for detection of the visible emission. A 400 nm long-pass filter (Thorlabs) was inserted at the emission side of the DAPI cube in order to allow for the detection of the visible emission, while cutting off the excitation wavelength.

The photoluminescence spectra in the NIR spectral range were recorded at room temperature with a modular double grating excitation spectrofluorimeter with a TRIAX 320 emission monochromator (Fluorolog-3, Horiba Scientific) coupled to a H9170 Hamamatsu photomultiplier, using a front face acquisition mode. The excitation source was a 450 W Xe arc lamp. The emission spectra were corrected for detection and optical spectral response of the spectrofluorimeter and the excitation spectra were corrected for the spectral distribution of the lamp intensity using a photodiode reference detector.

Data analysis and plotting were performed with the instrument's PHySpecV2 software as well as Origin Pro®.

Energy transfer modeling

Based on all equations regarding the energy transfer rates (Eqs. (S4)–(S13), ESI section) and Scheme 2 below, we introduce the concept of the balance of the non-radiative energy transfer rates for an individual pathway I at the temperature T, $W_i^*(T)$:

$$W_i^*(T) = W_i - W_i e^{-\left(\frac{|\Delta|}{k_B T}\right)} \quad \text{if } \Delta > 0 \qquad (2)$$

$$W_i^*(T) = W_i e^{-\left(\frac{|\Delta|}{k_B T}\right)} - W_i \quad \text{if } \Delta < 0 \qquad (3)$$

where $e^{-\left(\frac{|\Delta|}{k_B T}\right)}$ is the energetic barrier factor (k_B is the Boltzmann constant). Depending on the signal of Δ, the energy transfer can occur preferably from the donors to the acceptors (when $\Delta > 0$, Eq. (2) and Scheme 2A) or the inverse situation (when $\Delta < 0$, Eq. (3) and Scheme 2B).

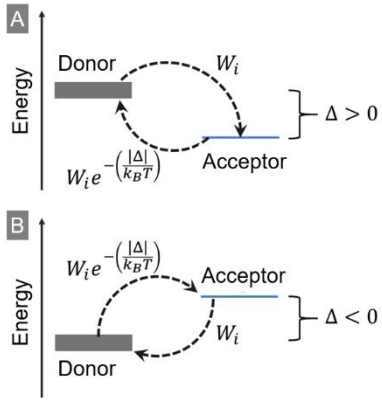

Scheme 2. Energetic situations where energy transfer can occur. A: Δ>0 and B: Δ<0.

Now, we can define the total balance W^* as a sum over all pathways and taking into consideration the Δ conditions by the simple form:

$$W^*(T) = \sum_i W_i^*(T) = \sum_i \frac{\Delta_i}{|\Delta_i|} W_i \left(1 - e^{-\left(\frac{|\Delta_i|}{k_B T}\right)}\right) \quad (4)$$

where the ratio $\Delta_i/|\Delta_i| = \pm 1$ is the factor that satisfies the conditions illustrated in Figure 1 and Eqs. (2) and (3). W_i is the sum of all mechanisms in the *i*-th pathway.

This theoretical model considers all possible energy transfer pathways between ligand and metal (or between metal centers). The sign, magnitude and thermal dependence of the total energy transfer rate resulting from the sum over each pathway afford an accurate description of the spectroscopic behavior of the luminescent systems under study.

Temperature uncertainty calculation

Temperature uncertainty (δT) associated to the thermal readouts was obtained considering the uncertainty associated with the thermometric parameter as:

$$\delta LIR = \sqrt{\left(\frac{-I_2}{{I_1}^2}\delta I_1\right)^2 + \left(\frac{1}{I_1}\delta I_2\right)^2} \quad (5)$$

where δI_1 and δI_2 are the uncertainties associated to of I_1 and I_2, respectively. δI_1 and δI_2 were determined considering the standard error (SE) of the mean value of the noise signal of the spectrum (measured in the 1150-1250 nm range):

$$SE = \frac{\sigma}{\sqrt{N}} \quad (6)$$

where σ is the standard derivation and N is the number of points. N is 201 for Nd-MOF doped with 5% Yb^{3+} and 101 for Nd MOFs doped with 1 and 2.5% Yb^{3+}.

Finally, temperature uncertainty (δT) was derived as follows:

$$\delta T = \frac{1}{S_r}\left|\frac{\delta LIR}{LIR}\right| \quad (7)$$

ASSOCIATED CONTENT

This material is available free of charge via the Internet at http://pubs.acs.org.

Electronic Supporting Information

Reaction conditions, ORTEP thermal ellipsoid plots, powder XRD patterns, thermal analysis data, SEM images, theoretical methodology, ESI (PDF). Accession Codes CCDC 1937198−1937201 contain the supplementary crystallographic data for this paper. These data can be obtained free of charge via www.ccdc.cam.ac.uk/data_request/cif, or by emailing data_request@ccdc.cam.ac.uk, or by contacting The Cambridge Crystallographic Data Centre (CCDC), 12 Union Road, Cambridge CB2 1EZ, UK; fax: +44 1223 336033.

AUTHOR INFORMATION

Corresponding Authors

*gegomez@unsl.edu.ar,
m.murugesu@uottawa.ca,
galo.soler.illia@gmail.com

Author Contributions

All authors have given approval to the final version of the manuscript.

ACKNOWLEDGMENTS

This study was supported by the MINCyT-UOttawa Project "*Optomagnetic Metal-Organic and Metal-Metalloporphyrin Frameworks*" Ot/14/03 (Ministerio de Ciencia, Tecnología e Innovación Productiva-University of Ottawa) and by MinCyT-ANPCyT projects PICT 2015-3526, PICT 2017 –4651 and PICT 2018-04236. We are grateful to the University of Ottawa, Natural Sciences and Engineering Research Council of Canada and Canada Foundation for Innovation.

G.E.G. thanks to CONICET (Consejo Nacional de Investigaciones Científicas y Técnicas) for the financing and Carolina Cerizola for her inconditionally support.

SYNOPSIS ToC: Novel heterometallic MOFs for solid state-lighting and near-infrared thermometry over a broad temperature range

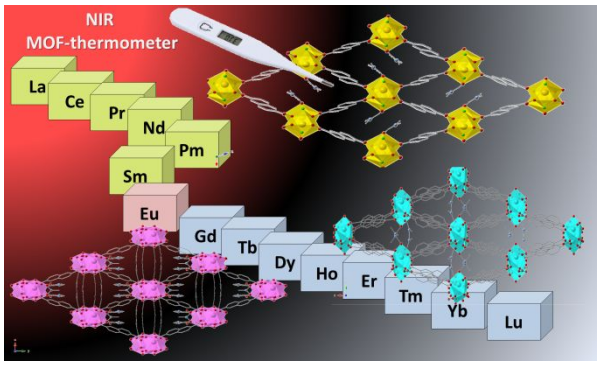

REFERENCES

[1] M. O'Keeffe, O. M. Yaghi, Deconstructing the Crystal Structures of Metal–Organic Frameworks and Related Materials into Their Underlying Nets, *Chem. Rev*, 2012, 112, 675-702.
[2] G. E. Gomez, J. A. Ridenour, N. M. Byrne, A. P. Shevchenko, C. L. Cahill, Novel Heterometallic Uranyl-Transition Metal Materials: Structure, Topology, and Solid State Photoluminescence Properties, *Inorg. Chem*, 2019, 58, 7243-7254.
[3] N. L. Rosi, J. Eckert, M. Eddaoudi, D. T. Vodak, J. Kim, M. O'Keeffe and O. M. Yaghi, Hydrogen storage in microporous metal-organic frameworks, *Science*, 2003, 300, 1127.
[4] J. Heine, K. Müller-Buschbaum, Engineering metal-based luminescence in coordination polymers and metal–organic frameworks, *Chem. Soc. Rev*., 2013, 42, 9232-9242.
[5] A. Corma, H. García, F. X. Llabrés i Xamena, Engineering Metal Organic Frameworks for Heterogeneous Catalysis, *Chem. Rev*., 2010, 110, 4606-4655.
[6] J.-L. Wang, C. Wang, W. Lin, Metal–Organic Frameworks for Light Harvesting and Photocatalysis, *ACS Catal.*, 2012, 2, 2630-2640.
[7] J.-R. Li, J. Sculley, H.-C. Zhou, Metal–Organic Frameworks for Separations, *Chem. Rev*., 2012, 112, 869-932.
[8] P. Horcajada, T. Chalati, C. Serre, B. Gillet, C. Sebrie, T. Baati, J. F. Eubank, D. Heurtaux, P. Clayette, C. Kreuz, J. S. Chang, Y. K. Hwang, V. Marsaud, P. N. Bories, L. Cynober, S. Gil, G. Férey, P. Couvreur, R. Gref, Porous metal-organic-framework nanoscale carriers as a potential platform for drug delivery and imaging, *Nat. Mater.*, 2010, 9, 172–178.
[9] Q. L. Zhu, Q. Xu, *Chem. Soc. Rev*., 2014, 43, 5468-5512.
[10] S. M. Cohen, Postsynthetic Methods for the Functionalization of Metal–Organic Frameworks, *Chem. Rev*., 2012, 112, 970-1000.
[11] L. E. Kreno, K. Leong, O. K. Farha, M. Allendorf, R. P. Van Duyne, J. T. Hupp, Metal–Organic Framework Materials as Chemical Sensors, *Chem. Rev.*, 2012, 112, 1105-1125.
[12] Y. Cui, B. Chen, G. Qian, Lanthanide metal-organic frameworks for luminescent sensing and light-emitting applications, *Coord. Chem. Rev*., 2014, 273-274, 76-86.
[13] X. Yang, X. Lin, Y. Zhao, Y. S. Zhao, D. Yan, Lanthanide Metal-Organic Framework Microrods: Colored Optical Waveguides and Chiral Polarized Emission, *Angew. Chem. Int. Ed*., 2017, 56, 7853-7857.
[14] Y. Gao, P. Jing, N. Yan, M. Hilbers, H. Zhang, G. Rothenberg, S. Tanase, Dual-mode humidity detection using a lanthanide-based metal–organic framework: towards multifunctional humidity sensors, *Chem. Commun.*, 2017, 53, 4465-4468.
[15] S. E. Miller, M. H. Teplensky, P. Z. Moghadam, D. Fairen-Jimenez, Metal-organic frameworks as biosensors for luminescence-based detection and imaging, Interface Focus 6: 20160027. https://doi.org/10.1098/rsfs.2016.0027.
[16] J. Dong, D. Zhao, Yi Lu, W.-Y. Sun, Photoluminescent metal–organic frameworks and their application for sensing

biomolecules, *J. Mater. Chem. A*, 2019,7, 22744-22767.
[17] J. Rocha, C, D. S. Brites, L. D. Carlos, Lanthanide Organic Framework Luminescent Thermometers, *Chem. Eur. J.*, 2016, 22, 14782-14795.
[18] G. E. Gomez, M. dos Santos Afonso, H. A. Baldoni, F. Roncaroli, G. J. A. A. Soler-Illia, Luminescent Lanthanide Metal Organic Frameworks as Chemosensing Platforms towards Agrochemicals and Cations, *Sensors*, 2019, 19, 1260-1275.
[19] S. Pramanik, C. Zheng, X. Zhang, T. J. Emge, J. Li, New microporous metal-organic framework demonstrating unique selectivity for detection of high explosives and aromatic compounds, *J. Am. Chem. Soc*., 2011, 133, 4153–4155.
[20] B. Chen, L. Wang, F. Zapata, G. Qian, E. B. Lobkovsky, A Luminescent Microporous Metal−Organic Framework for the Recognition and Sensing of Anions, *J. Am. Chem. Soc*., 2008, 130, 6718–6719.
[21] B. Chen, Y. Yang, F. Zapata, G. Lin, G. Qian, E. B. Lobkovsky, Luminescent open metal sites within a metal-organic framework for sensing small molecules, *Adv. Mater*., 2007, 19, 1693–1696.
[22] Y. Cui, F. Zhu, B. Chen, G. Qian, Metal–organic frameworks for luminescence thermometry, *Chem. Commun*., 2015, 51, 7420-7431.
[23] C. D. S. Brites, P. P. Lima, N. J. O. Silva, A. Millán, V. S. Amaral, F. Palacio, L. D. Carlos, Thermometry at the nanoscale, *Nanoscale*, 2012, 4, 4799–4829.
[24] X. Rao, T. Song, J. Gao,Y. Cui,Y. Yang, C. Wu, B. Chen, G. Qian, A Highly Sensitive Mixed Lanthanide Metal–Organic Framework Self-Calibrated Luminescent Thermometer, *J. Am. Chem. Soc.* 2013, 135, 41, 15559-15564.
[25] Z. Wang, D. Ananias, A. Carné-Sánchez, C. D. S. Brites, I. Imaz, D. Maspoch, J. Rocha, L. D. Carlos, Lanthanide–Organic Framework Nanothermometers Prepared by Spray□Drying, *Adv. Funct. Mater.*, 2015, 25, 2824-2830.
[26] L. Li, Y. Zhu, X. Zhou, C. D. S. Brites, D. Ananias, Z. Lin, F. A. Almeida Paz, J. Rocha, W. Huang, L. D. Carlos, Visible□Light Excited Luminescent Thermometer Based on Single Lanthanide Organic Frameworks, *Adv. Funct. Mater.*, 2016, 26, 8677-8684.
[27] C. D. S. Brites, P. P. Lima, N. J. O. Silva, A. Millan, V. S. Amaral, F. Palacio, L. D. Carlos, A luminescent molecular thermometer for long-term absolute temperature measurements at the nanoscale, *Adv. Mater.*, 2010, 22, 4499–4504.
[28] A. Cadiau, C. D. S. Brites, P. M. F. J. Costa, R. A. S. Ferreira, J. Rocha, L. D. Carlos, Ratiometric nanothermometer based on an emissive Ln^{3+}-organic framework, *ACS Nano*, 2013, 7, 7213–7218.
[29] M. Ren, C. D. S. Brites, S.-S. Bao, R. A. S. Ferreira, L.-M. Zheng, L. D. Carlos, A cryogenic luminescent ratiometric thermometer based on a lanthanide phosphonate dimer, *J. Mater. Chem. C*, 2015, 3, 8480–8484.
[30] Y. Cui, H. Xu, Y. Yue, Z. Guo, J. Yu, Z. Chen, J. Gao, Y. Yang, V. Qian, B. A. Chen, A Luminescent Mixed-Lanthanide Metal–Organic Framework Thermometer, *J. Am. Chem. Soc*. 2012, 134, 3979–3982.
[31] X. T. Rao, T. Song, J. K. Gao, Y. J. Cui, Y. Yang, C. D. Wu, B. L. Chen, G. D. Qian, A Highly Sensitive Mixed Lanthanide Metal–Organic Framework Self-Calibrated Luminescent Thermometer, *J. Am. Chem. Soc*. 2013, 135, 15559–15564.
[32] Y. Cui, W. Zou, R. Song, J. Yu, W. Zhang, 681 Y. Yang, G. Qian, A ratiometric and colorimetric luminescent thermometer over a wide temperature range based on a lanthanide coordination polymer, *Chem. Commun*. 2014, 50, 719–721.
[33] Y. Cui, R. Song, J. Yu, M. Liu, Z. Wang, C. Xu, Y. Yang, Z. Wang, B. Chen, G. Qian, Dual-emitting MOF⊃dye composite for ratiometric temperature sensing, *Adv. Mater*. 2015, 27, 1420–1425.
[34] G. E. Gomez, A. M. Kaczmarek, R. V. Deun, E. V. Brusau, G. E. Narda, D. Vega, M. Iglesias, E. Gutierrez-Puebla, M. A. Monge, Photoluminescence, unconventional-range temperature sensing, and efficient catalytic activities of lanthanide metal–organic frameworks, *Eur. J. Inorg. Chem*., 2016, 1577–1588.
[35] A. A. Godoy, G. E. Gomez, A. M. Kaczmarek, R. Van Deun, O. J. Furlong, F. Gándara, M. A. Monge, M. C. Bernini, G. E. Narda, Sensing properties, energy transfer mechanism and tuneable particle size processing of luminescent two-dimensional rare earth coordination networks, *J. Mater. Chem. C*, 2017, 5, 12409-12421.
[36] A. Foucault-Collet, K. A. Gogick, K. A. White, S. Villette, A. Pallier, G. Collet, C. Kieda, T. Li, S. J. Geib, N. L. Rosi, S. Petoud, Lanthanide near infrared imaging in living cells with Yb^{3+} nano metal organic frameworks, *PNAS*, 2013, 43, 17199-17204.
[37] D.Yue, J. Zhang, D. Zhao, X. Lian,Y. Cui, Y. Yang, G. Qian, Ratiometric near infrared luminescent thermometer based on lanthanide metal-organic frameworks, *J. Sol. State. Chem*., 2016, 241, 99-104.
[38] D. Ananias, F. A. A: Paz, L. D. Carlos, J. Rocha, Near□Infrared Ratiometric Luminescent Thermometer Based on a New Lanthanide Silicate, *Chem. Eur. J.*, 2018, 24, 11926-11935.
[39] C. Liu, S. V. Eliseeva, T.-Y. Luo, P. F. Muldoon, S. Petoud, N. L. Rosi, Near infrared excitation and emission in rare earth MOFs via encapsulation of organic dyes, *Chem. Sci.*, 2018, 9, 8099-8102.

[40] D. Ruiz, B. del Rosal, M. Acebrón, C. Palencia, C. Sun, J. Cabanillas-González, M. López-Haro, A. B. Hungría, D. Jaque, B. H. Juarez, Ag/Ag_2S Nanocrystals for High Sensitivity Near□Infrared Luminescence Nanothermometry, *Adv. Funct. Mater.* 2017, 1604629.
[41] R. Weissleder, A clearer vision for in vivo imaging, *Nat. Biotechnol*. 2001, 19, 316-317.
[42] E. C. Ximendes, U. Rocha, T. O. Sales, N. Fernández, F. Sanz-Rodríguez, I. R. Martín, C. Jacinto, D. Jaque, In Vivo Subcutaneous Thermal Video Recording by Supersensitive Infrared Nanothermometers, *Adv. Funct. Mater.* 2017, 1702249. https://doi.org/10.1002/adfm.201702249.
[43] S. Diao, G. Hong, A. L. Antaris, J. L. Blackburn, K. Cheng, Z. Cheng, H. Dai, Biological imaging without autofluorescence in the second near-infrared region, *Nano Res*. 2015, 8, 3027-3034.
[44] E. Hemmer, N. Venkatachalam, H. Hyodo, A. Hattori, Y. Ebina, H. Kishimoto, K. Soga, Upconverting and NIR emitting rare earth based nanostructures for NIR-bioimaging, *Nanoscale,* 2013, 5, 11339-11361.
[45] B. del Rosal, I. Villa, D. Jaque, F. Sanz-Rodríguez, In vivo autofluorescence in the biological windows: the role of pigmentation, *J. Biophotonics*, 2016, 9, 1059-1067.
[46] I. Villa, A. Vedda, I. X. Cantarelli, M. Pedroni, F. Piccinelli, M. Bettinelli, A. Speghini, M. Quintanilla, F. Vetrone, U. Rocha, C. Jacinto, E. Carrasco, F. S. Rodríguez, Á. Juarranz, B. del Rosal, D. H. Ortgies, P. H. Gonzalez, J. G. Solé, D. J. García, 1.3 μm emitting SrF_2:Nd^{3+} nanoparticles for high contrast in vivo imaging in the second biological window*, Nano Res*. 2015, 8, 649-665.
[47] Y.-H. Liu, P.-H. Chien, A series of lanthanide–organic frameworks possessing arrays of 2D intersecting channels within a 3D pillar-supported packed double-decker network and Co^{2+}-induced luminescence modulation, *CrystEngComm*, 2014, 16, 8852-8862.
[48] Y. Zhu, L. Wang, X. Chen, P. Wang, Y. Fan, P. Zhang, 3D lanthanide metal-organic frameworks constructed from 2,6-naphthalenedicarboxylate ligand: synthesis, structure, luminescence and dye adsorption, *J. of Solid State Chemistry*, 2017, 251, 248-254.
[49] C.-C. Wang, C.-T. Yeh, S.-Y. Ke, Y.-T. Cheng, Assembly of three Nd(III) 2,6-naphthalenedicarboxylates (ndc^{2-}) 3D coordination polymers based on various secondary building units (SBUs): structural diversity and gas sorption properties, *RSC Adv*., 2015, 5, 92378-92386.
[50] Y.-B. Lu, S. Jin, Z.-G. Zhou, S.-Y. Zhang, G.-T. Lou, Y.-R. Xie, The syntheses, structures, magnetic and luminescent properties of five new lanthanide(III)–2,6-naphthalenedicarboxylate complexes, *Inorg. Chem. Comm.*, 2014, 48, 73–76.
[51] R. Łyszczek, Z. Rzączyńska, A. Kula, A. Gładysz-Płaska, Thermal and luminescence characterization of lanthanide 2,6-naphthalenedicarboxylates series, *J. of Anal. And Appied Pyrolisis*, 2011, 92, 347-354.
[52] R. Łyszczek, A. Lipke, Microwave-assisted synthesis of lanthanide 2,6-naphthalenedicarboxylates: Thermal, luminescent and sorption characterization, *Microporous and Mesoporous Materials*, 168, 2013, 81-91.
[53] W. Lu, Z. Wei, Z.-Y. Gu, T.-F. Liu, J. Park, J. Park, J. Tian, M. Zhang, Q. Zhang, T- Gentle III, M. Bosch, H.-C. Zhou, Tuning the structure and function of metal–organic frameworks via linker design, *Chem. Soc. Rev*., 2014, 43, 5561-5593.
[54] G. E. Gomez, M. C. Bernini, E. V. Brusau, G. E. Narda, W. A. Massad, Ana Labrador, Two Sets of Metal Organic Frameworks along the Lanthanide Series Constructed by 2,3-Dimethylsuccinate: Structures, Topologies, and Strong Emission without Ligand Sensitization, *Cryst. Growth Des*., 2013, 13, 5249−5260.
[55] M. C. Bernini, F. Gándara, M. Iglesias, N. Snejko, E. Gutiérrez-Puebla, E. V. Brusau, G. E. Narda, M. A. Monge, Reversible breaking and forming of metal-ligand coordination bonds: temperature-triggered single-crystal to single-crystal transformation in a metal-organic framework, *Chem. Eur. J*., 2009, 15, 4896 – 4905.
[56] C. F. Macrae, I. J. Bruno, J. A. Chisholm, P. R. Edgington, P. McCabe, E. Pidcock, L. Rodriguez-Monge, R. Taylor, J. Van De Streek, P. A. Wood, Mercury CSD 2.0 – new features for the visualization and investigation of crystal structures, *J. Appl. Cryst.*, 2008, 41, 466-470.
[57] M. Thommes, K. Kaneko, A. V. Neimark, J. P. Olivier, F. Rodriguez-Reinoso, J. Rouquerol and Kenneth S.W. Sing, Physisorption of gases, with special reference to the evaluation of surface area and pore size distribution (IUPAC Technical Report), *Pure and Applied Chemistry*, 2015. 87, 1051-1069.
[58] V. A. Blatov, A. P. Shevchenko, D. M. Proserpio, Applied Topological Analysis of Crystal Structures with the Program Package ToposPro, *Cryst. Growth Des*., 2014, 14, 3576-3586.
[59] M. C. Bernini, G. E. Gomez, E. V. Brusau, G. E. Narda, Reviewing Rare Earth Succinate Frameworks from the Reticular Chemistry Point of View: Structures, Nets, Catalytic and Photoluminescence Applications, *Isr. J. Chem.,* 2018, 58, 1044 – 1061.
[60] N. L. Rosi, J. Kim, M. Eddaoudi, B. Chen, M. O'Keeffe, O. M. Yaghi, Rod Packings and Metal−Organic Frameworks Constructed from Rod-Shaped Secondary Building Units, *J. Am. Chem. Soc*., 2005, 127, 1504-1518.

[61] M. Li, D. Li, M. O'Keeffe, O. M Yaghi, Topological analysis of metal-organic frameworks with polytopic linkers and/or multiple building units and the minimal transitivity principle, *Chem. Rev.*, 2014, 114, 1343-1370.
[62] C. Bonneau, M. O'Keeffe, D. M. Proserpio, V. A. Blatov, S. R. Batten, S. A. Bourne, M. Soo Lah, J.-G. Eon, S. T. Hyde, S. B. Wiggin, L. Öhrström, Deconstruction of Crystalline Networks into Underlying Nets: Relevance for Terminology Guidelines and Crystallographic Databases, *Crystal Growth & Design*, 2018, 18, 6, 3411-3418.
[63] H. K. Chae, M. Eddaoudi, J. Kim, S. I. Hauck, J. F. Hartwig, M. O'Keeffe, O. M Yaghi, Tertiary Building Units: Synthesis, Structure, and Porosity of a Metal−Organic Dendrimer Framework (MODF-1), *J. Am. Chem. Soc*., 2001, 123, 11482-11483.
[64] A. J. Cairns, J. A. Perman, L. Wojtas, V. C. Kravtsov, M. H. Alkordi, M. Eddaoudi, M. J. Zaworotko, Supermolecular building blocks (SBBs) and crystal design: 12-connected open frameworks based on a molecular cubohemioctahedron, *J. Am. Chem. Soc*., 2008, 130, 1560-1561.
[65] O. L. Malta, H. F. Brito, J. F. S. Menezes, F. R. Gonçalves e Silva, S. Alves Jr., F. S. Farias Jr., A. V. M. De Andade, Spectroscopic properties of a new light-converting device Eu(thenoyltrifluoroacetonate)$_3$2(dibenzyl sulfoxide). A theoretical analysis based on structural data obtained from a sparkle model, *J. Lumin.,* 1997, 75 (3), 255-268.
[66] O. L. Malta, F. R. A. Gonçalves e Silva, A theoretical approach to intramolecular energy transfer and emission quantum yields in coordination compounds of rare earth ions, *Spectrochim. Acta Part A Mol. Biomol. Spectrosc.,* 1998, 54 (11), 1593–1599.
[67] R. Longo, F. R. A. Gonçalves Silva, O. L. Malta, A theoretical study of the energy-transfer process in [Eu⊂bpy.bpy.bpy]$^{3+}$ cryptates: a ligand-to-metal charge-transfer state?, *Chem. Phys. Lett.* 2000, *328* (1–2), 67–74;
[68] O. L. Malta, Mechanisms of non-radiative energy transfer involving lanthanide ions revisited, *J. Non. Cryst. Solids* 2008, 354(42–44), 4770–4776.
[69] F. R. G. e Silva, F. R. G., O. L. Malta, Calculation of the ligand–lanthanide ion energy transfer rate in coordination compounds: contributions of exchange interactions, *J. Alloys Compd.*, 1997, 250 (1–2), 427–430.
[70] H. F. Brito, O. M. L. Malta, M. C. F. C. Felinto, E. E. S. Teotonio, Luminescence Phenomena Involving Metal Enolates. In *The chemistry of Metal Enolates*; ZABICKY, J., Ed.; Wiley-VCH Verlag GmbH: Weinheim, Germany, 2009.
[71] A. N. Carneiro Neto, E. E. S. Teotonio, G. F. de Sá, H. F. Brito, J. Legendziewicz, L. D. Carlos, M. C. F. C. Felinto, P. Gawryszewska R. T. Moura Jr., R. L. Longo, Modeling Intramolecular Energy Transfer in Lanthanide Chelates: A Critical Review and Recent Advances. In *Handbook on the Physics and Chemistry of Rare Earths*; Elsevier, 2019, 55–162.
[72] A. N. Carneiro Neto, R. T. Moura, O. L. Malta, On the mechanisms of non-radiative energy transfer between lanthanide ions: centrosymmetric systems, *J. Lumin.,* 2019, 210, 342–347.
[73] L. D. Sun, Y. F. Wang, C. H. Yan, Paradigms and Challenges for Bioapplication of Rare Earth Upconversion Luminescent Nanoparticles: Small Size and Tunable Emission/Excitation Spectra, *Acc. Chem. Res*., 2014, 47, 1001-1009.
[74] C. Chen, C. Li, Z. Shi, Current Advances in Lanthanide-Doped Upconversion Nanostructures for Detection and Bioapplication, *Adv. Sci*., 2016, 3, 1600029.
[75] A. M. Smith, M. C. Mancini, S. Nie, Bioimaging: second window for in vivo imaging, *Nat. Nanotechnol*., 2009, 4, 710-711.
[76] X. Zhang, F. Ai, T. Sun, F. Wang, G. Zhu, Multimodal Upconversion Nanoplatform with a Mitochondria-Targeted Property for Improved Photodynamic Therapy of Cancer Cells, *Inorg. Chem*., 2016, 55, 3872-3880.
[77] A. Skripka, V. Karabanovas, G. Jarockyte, R. Marin, V. Tam, M. Cerruti, R. Rotomskis, F. Vetrone, Decoupling Theranostics with Rare Earth Doped Nanoparticles, *Adv. Funct. Mater*. 2019, 29, 1807105.
[78] B. Liu, C. Li, P. Yang, Z. Hou, J. Lin, In Vivo Subcutaneous Thermal Video Recording by Supersensitive Infrared Nanothermometers, *Adv. Funct. Mater.,* 2017, 1702249.
[79] L. D. Merkle, M. Dubinskii, K. L. Schepler, S. M. Hegde, Concentration quenching in fine-grained ceramic Nd:YAG, *Opt. Exp*., 2006, 14, 3893-3905.
[80] B. Xu, D. Li, Z. Huang, C. Tang, W. Mo, Y. Ma, Alleviating luminescence concentration quenching in lanthanide doped CaF_2 based nanoparticles through Na^+ ion doping, *Dalton Trans.*, 2018, 47, 7534-7540.
[81] Ł. Marciniak, A. Bednarkiewicz, M. Stefanski, R. Tomala, D. Hreniaka,W. Strek, Near infrared absorbing near infrared emitting highly-sensitive luminescent nanothermometer based on Nd^{3+} to Yb^{3+} energy transfer, *Phys. Chem. Chem. Phys*., 2015, 17, 24315-24321.
[82] A. D. Sontakke, K. Biswas, R. Sen, K. Annapurna, Efficient non-resonant energy transfer in Nd^{3+}-Yb^{3+} codoped Ba-Al-metaphosphate glasses, *J. Opt. Soc. of Am. B*, 2010, 27, 2750-2758.
[83] A. Benayas, B. del Rosal, A. Pérez-Delgado, K. Santacruz-Gómez, D. Jaque, G. Alonso Hirata, F. Vetrone, Nd:YAG Near-Infrared Luminescent Nanothermometers, *Adv. Opt. Mater.*, 2015, 3, 687-694.

[84] A. Skripka, A. Morinvil, M. Matulionyte, T. Cheng, F. Vetrone, Advancing neodymium single-band nanothermometry, *Nanoscale*, 2019, 11, 11322-11330.
[85] P. Huang, W. Zheng, D. Tu, X. Shang, M. Zhang, R. Li, J. Xu,Y. Liu, X. Chen, Unraveling the Electronic Structures of Neodymium in LiLuF4 Nanocrystals for Ratiometric Temperature Sensing, *Adv. Sci*., 2019, 6, 2019, 1802282.
[86] A. M. Tkachuk, S. É. Ivanova, L. I. Isaenko, A. P. Yelisseyev, S. Payne, R. Solarz, R. Page, M. Nostrand, Spectroscopic study of neodymium-doped potassium-lead double chloride Nd^{3+}:KPb_2Cl_5 crystals, *Opt. Spectrosc*., 2002, 92, 83–94.
[87] C. D. S. Brites, A. Millán, L. D. Carlos, Handbook on the Physics and Chemistry of Rare Earths, 2016, 49, 339-427.
[88] Crystal Maker; Crystal Maker Software Limited: Bicester, England, 2009.